An Adaptive Blended Algorithm Approach for Deriving Bathymetry from Multispectral Imagery

Yongming Liu, Danling Tang , Ruru Deng, Bin Cao, Qidong Chen, Ruihao Zhang, Yan Qin, and Shaoquan Zhang

Abstract—The log-ratio method (LRM) proposed by Stumpf *et al.* has been widely used to map bathymetry from multispectral imagery for oligotrophic waters, while the selection criteria of bands for the LRM have been subject to tradeoffs between maximum detectable depth and sensitivity. In this article, we first applied a method for global sensitivity analysis to a semianalytical forward model of optically shallow waters with the WorldView-2 band-set. The results show that the sensitive wavelength band in water-leaving reflectance for water depth varies from the longer wavelength band to the shorter wavelength band with increasing water depth. Then, we developed an adaptive blended algorithm approach (ABAA) to seamlessly map bathymetry from the shallower region to the deeper region. The LRM with different band combinations was selected for the sub-algorithms of the ABAA. The subalgorithms and depth range used for each subalgorithm of the ABAA were automatically determined by the proposed applicable depth range analysis that considers logarithmic regression for the LRM. The ABAA was applied to WorldView-2 and Landsat-8 imagery of the Xisha Qundao. When the *in situ* bathymetry data are available, compared with the LRM with the blue and green bands, the ABAA significantly improves the accuracy of the estimated depth, especially for waters shallower than 6 m (root–mean- square error (RMSE) = 0.31 to 0.94 m for WorldView-2 data, RMSE= 0.25 to 1.42 m for Landsat-8 data). When the *in situ* bathymetry data are absent, the ABAA performs better than the LRM with a single band ratio and an optimization-based method overall.

Index Terms—Bathymetry, coral reef, sensitivity analysis, shallow water.

Yongming Liu is with the Guangdong Key Laboratory of Ocean Remote Sensing, State Key Laboratory of Tropical Oceanography, South China Sea Institute of Oceanology, Chinese Academy of Sciences, Guangzhou 510301, China, and also with Southern Marine Science and Engineering Guangdong Laboratory, Guangzhou 511458, China (e-mail: liuyongminga401@outlook.com).

Danling Tang is with the Southern Marine Science and Engineering Guangdong Laboratory, Guangzhou 511458, China, and also with Guangdong Key Laboratory of Ocean Remote Sensing, State Key Laboratory of Tropical Oceanography, South China Sea Institute of Oceanology, Chinese Academy of Sciences, Guangzhou 510301, China (e-mail: lingzistdl@126.com).

Ruru Deng, Bin Cao, and Ruihao Zhang are with the School of Geography and Planning, Sun Yat-sen University, Guangzhou 510275, China (e-mail: eesdrr@mail.sysu.edu.cn; caobinalonzo@sina.com; 893101762@qq.com).

Qidong Chen is with the South China Sea Institute of Planning and Environmental Research, State Oceanic Administration, Guangzhou 510300, China (e-mail: 99810961@qq.com).

Yan Qin is with the Guangdong Research Institute of Water Resources and Hydropower, Guangzhou 510630, China (e-mail: qin.yan@foxmail.com).

Shaoquan Zhang is with the Jiangxi Province Key Laboratory of Water Information Cooperative Sensing and Intelligent Processing, Nanchang Institute of Technology, Nanchang 330099, China.

Digital Object Identifier 10.1109/JSTARS.2020.3034375

I. INTRODUCTION

CORAL reefs are among the most productive and biologically diverse ecosystems on earth [1]. Mapping the bathymetry of coral reefs aids in managing and protecting coral reefs [2]. Ship-based echosounder and airborne LiDAR bathymetry are traditionally used for measuring the bathymetry of coral reefs. In addition, satellite-based multispectral remote sensing technology, which carries the advantages of a high platform and low cost, has demonstrated the potential to map bathymetry from optically shallow waters [3]–[8].

Multispectral remote sensing inversion models based on the radiative transfer theory can be classified into three types, namely look-up table methods, optimization-based methods and empirical methods [5], [7], [9], [10]. Empirical methods, such as the log-ratio method (LRM) [7] and log-linear method [11], which carry the advantages of relatively simple form and high computational efficiency, have been widely applied to satellite-based multispectral data. Among those empirical methods, the LRM is a widely used model due to its limited empirical parameters. The LRM is valid due to the different water absorptions of the two selected bands [7]. Generally, a band that is sensitive to depth change and a band that is not sensitive to depth change are selected [12]. In previous studies, nearly all the modified LRM for oligotrophic waters only used a single band ratio for the whole range of optically shallow regions [13]–[19]. A bands' selection criteria for the LRM has been subject to tradeoffs between maximum detectable depth and sensitivity. In theory, the LRM with the blue and red bands may perform better than the LRM with the blue and green bands in very shallow water because the red band or bands with longer wavelengths have stronger absorption than the green band or bands with shorter wavelengths [20], [21]. From a remote sensing perspective, whether water depth is the most or least important parameter in explaining the variation in water-leaving reflectance determines the selection of bands for estimating water depth [22]. Thus, we first carry out a sensitivity analysis for a semianalytical forward model of optically shallow water for oligotrophic waters [23].

Since most satellite-based multispectral data, whose spatial resolution is not lower than 30 m, have at least three bands in the visible domain, at least three different band ratios can be used to map bathymetry based on the LRM band selection criteria, such as IKONOS, WorldView-2 (WV2), Landsat-8 (L8), etc. Therefore, there is a need to build a blended algorithm approach to solve the problem where pixels within different water depth ranges need to be estimated by water depth with the optimal band ratio. When considering the entire dynamic range of environmental conditions, a blended algorithm approach is superior to single algorithms [24]. However, some issues are associated with the blended algorithm approach. Preliminary results of water depth should be derived first. State-of-the-art multispectral remote sensing inversion models indicate that the preliminary results of water depth can be estimated. The applicable depth range of sub-algorithms should be automatically determined based on the selected image or study region because the different water optical properties of different study regions may influence the applicable depth range [15]. The applicable depth range means the depth range to be used for a specific subalgorithm. To the best of our knowledge, the second issue remains unresolved. The results from sub-algorithms should be seamlessly merged. Although the third issue has not been solved in the research field of mapping bathymetry, similar issues in the research field of ocean color remote sensing have been resolved [25]–[27].

One of the major limitations of empirical methods is that *in situ* bathymetry data need to be collected to calibrate the empirical parameters. Recently, the limitation of empirical methods was overcome to a certain extent. The first solution type derived the water depth with other methods, such as the wave method or optimization-based method, which works without *in situ* bathymetric data but is often criticized due to the low spatial resolution or the time-consuming requirements of iterative computations, and then, the derived depth and the matched reflectance were used for calibration [17], [28]. The other solutions attempted to relate the empirical parameters to water properties and assumed that water properties are spatially homogeneous [15], [16], [29]. Finally, we would like to extend the blended algorithm approach to the condition where *in situ* bathymetry data are absent with the first kind of solution.

In this article, we first carried out a sensitivity analysis for a semianalytical forward model of optically shallow water for oligotrophic waters to understand the contribution of water depth to the variance of reflectance within different depth ranges in different bands. Further, we developed an adaptive blended algorithm approach (ABAA) to estimate water depth from satellite-based multispectral data with or without *in situ* bathymetry data. The LRM with optimal band ratios was selected for the subalgorithms of the ABAA. In particular, a solution for automatically determining the applicable depth range of each subalgorithm was provided.

II. METHODS

A. Overview

The flowchart of our approach is shown in Fig. 1. First, satellite data were reprocessed, including radiometric

TABLE I
SATELLITE-BASED IMAGERY DATA AND *In Situ* BATHYMETRY DATA USED IN THIS ARTICLE

Sensor name	Name of islands	Data ID or imaging time	In-situ bathymetry data
Landsat-8	Qilian Yu Yongxing Dao	LC81220482014176LGN00	Echo-sounder + GPS Depth range: 1–130 m
		LC81220482016166LGN00	
		LC81220482017200LGN00	
WorldView-2	Ganquan Dao	2015-10-25	SHOALS-3000 Depth range: 1–20 m
		2011-01-05	
		2019-07-15	

calibration, sun-glint correction and atmospheric correction. Second, subalgorithms (LRM with optimal band ratios) for the ABAA and corresponding applicable depth ranges were determined by our newly developed applicable depth range analysis (ADRA) with *in situ* bathymetry data or bathymetry results derived by an optimization-based method. Third, subalgorithms were used to estimate water depth, and bathymetry results estimated by subalgorithms were merged based on their applicable depth ranges. Finally, bathymetry results estimated by the ABAA were validated with *in situ* bathymetry data and compared with two existing methods.

B. Study Site and Data

We selected Qilian Yu, Ganquan Dao, and Yongxing Dao in the Xisha Qundao as our study sites (see Fig. 2). These three islands are all surrounded by optically shallow coral reefs. The area of Ganquan Dao is approximately 0.3 km². Qilian Yu is composed of seven small parts, namely Xisha Zhou, Bei Dao, Zhong Dao, Sanchi Zai, Beisha Zhou, Zhongsha Zhou, and Nansha Zhou, and the average area of each part is approximately 0.4 km². The area of Yongxing Dao is approximately 2.13 km². The euphotic depth can reach 120 m near the Xisha Qundao [30], and the Xisha Qundao are suitable for the study of bathymetric mapping by optical remote sensing technology.

The new method was applied to WV2 and L8 data. WV2 imagery contains six bands in the visible range (coastal band, blue, green, yellow, red, and red-edge band) and nine near-infrared (NIR) bands. The spatial resolution of WV2 is 2 m in the multispectral mode. Three WV2 images that cover Ganquan Dao were used in this study. L8 contains eight bands whose spatial resolutions are 30 m, namely four visible bands (coastal, blue, green and red band), one NIR band, two shortwave infrared bands and a cirrus band. L8 data are available free of charge via the website of the United States Geological Survey.[1] Three L8 images covering Qilian Yu and Yongxing Dao were used for the validation of our new method. Table I gives the satellite data and *in situ* bathymetry data used in this article.

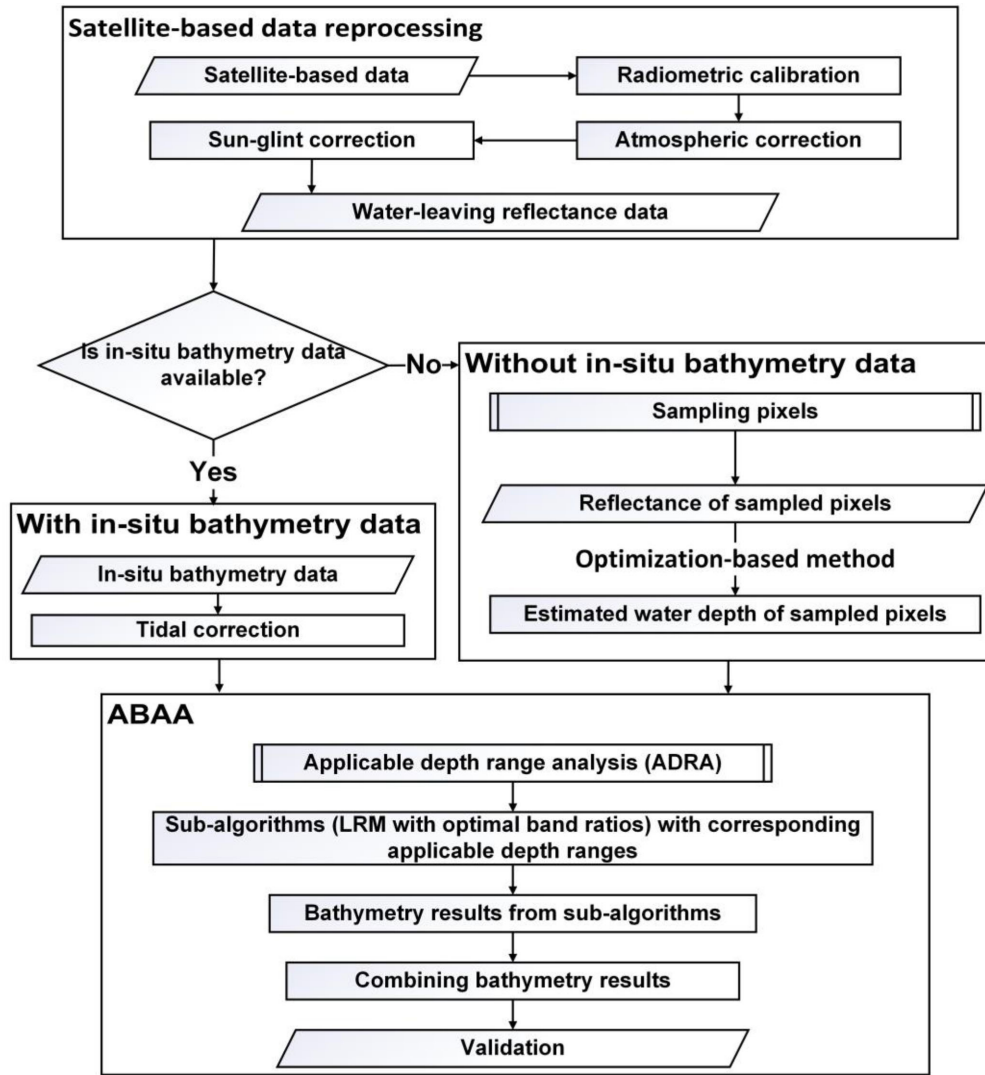[1] Online. [Available]: https://earthexplorer.usgs.gov/.

Fig. 1.   Image processing workflow to perform ABAA.

In situ bathymetry data were available for Ganquan Dao, Yongxing Dao and Qilian Yu [Red points in Fig. 2(c) and (d)]. Bathymetric LiDAR data were collected with SHOALS-3000 (CO., OPTECH) at Ganquan Dao in 2013. The vertical accuracy of bathymetric LiDAR data is 0.25 m. *In situ* bathymetry data were collected at Qilian Yu and Yongxing Dao with a multibeam sonar (CO., SOUTH) in 2013. The geolocation of the sonar data was tracked by a Global Positioning System device (CO., SOUTH). The vertical accuracy of sonar bathymetry data is $\pm 0.01 \pm 0.1\%H$ m (where H is the water depth). The vertical accuracy was taken from the manual of the multibeam sonar.

C. Preprocessing Phase

The new method will be applied to the water-leaving reflectance. After the radiometric calibration process, the preprocessing phase mainly included atmospheric correction and sun-glint correction.

1) Atmospheric Correction: An atmospheric correction scheme described in [31] was applied to the L8 imagery. Signals due to Rayleigh and aerosol scattering were taken as a whole in this scheme. First, contributions from the atmosphere and sea-surface reflectances were estimated by the reflectance of optically deep water under the sun and in the shadow. Second, the reflectance of clouds was considered to be independent of wavelength, and the reflectance of optically deep water in the green band was assumed to be known. The remaining unknowns were obtained to correct the signals due to Rayleigh and aerosol scattering in the other visible bands.

Since clouds with high reflectance are absent from our selected WV2 images, an atmospheric correction scheme described in [9] was used for WV2 imagery. The signal due to Rayleigh scattering was corrected first. Then, we corrected the upward and downward diffuse transmittances due to ozone absorption and Rayleigh scattering. Finally, the reflectance of adjacent optically deep water at the two NIR bands was assumed to be zero, and the aerosol optical depth of the two NIR
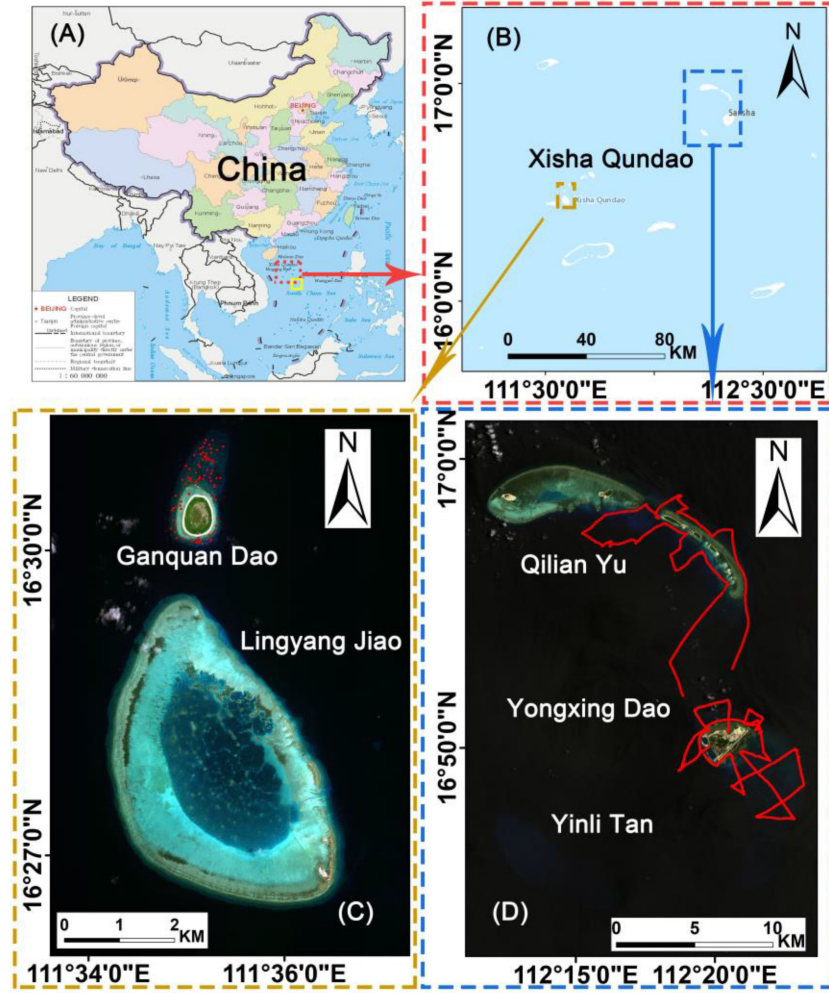
Fig. 2. (a) Location of Xisha Qundao. Yellow rectangle represents a region of optically shallow water near Xisha Qundao. (b) Locations of the two study sites. (c) True color image derived from a WV2 image of Ganquan Dao. Red points are the geolocations of LiDAR data (only a subset (1%) of Lidar data is presented). (d) True color image derived from a L8 image of Qilian Yu and Yongxing Dao. Red lines are the geolocations of ship-based sonar depth points.

bands was calculated. Provided that the aerosol optical depth in the visible-NIR range follows the Angstrom formula [32], the aerosol optical depth of visible bands was extrapolated from the NIR bands.

2) Sun-Glint Correction: We adopted the sun-glint correction scheme provided by Hedley *et al.* [33]. In the visible-NIR region, the specular reflectance of the water surface is independent of wavelength [34]; then the sun-glint of the visible band and the sun-glint of the NIR band are linearly related. Therefore, a small region of optically deep water is extracted from the imagery, and the minimum value ($R_{\mathrm{NIR\_min}}$) of the NIR band is obtained from statistics. Then, scatter plots between the visible and NIR band are plotted, and the ordinary least squares regression lines are calculated. The slope (b_i) of the regression line and $R_{\mathrm{NIR\_min}}$ are substituted into the formula below to correct for sun-glint

$$R'_i = R_i - b_i \left(R_{\mathrm{NIR}} - R_{\mathrm{NIR\_min}} \right) \tag{1}$$

where R'_i and R_i are the water-leaving reflectance of the visible band after and before sun-glint correction, respectively. R_{NIR} is the water-leaving reflectance of the NIR band. For WV2

imagery, the blue, green and red bands were corrected with NIR band 1. The coastal, yellow and red-edge bands were corrected with NIR band 2.

D. Global Sensitivity Analysis of the Forward Model of Optically Shallow Water

The Latin-hypercube-one-factor-at-a-time (LH-OAT) method, which is an extension of the one-factor-at-a-time method, was used to calculate the global sensitivity of the semianalytical model parameters. LH-OAT was first developed and applied to a global sensitivity analysis of the hydrology model by Griensven *et al.* [35]. Although LH-OAT has not been used for global sensitivity analysis of remote sensing models, one-factor-at-a-time is appropriate for continuous models [36], and the semianalytical model of optically shallow water is a continuous model. The band-set of WV2 was chosen as an example.

1) Semianalytical Forward Model of Optically Shallow Water: The subsurface remote reflectance of optically shallow

waters can be expressed as a function of the total absorption coefficient a, total backscattering coefficient b_b, sun zenith angle θ_ω, albedo of substratum ρ and water depth H [23] (we omit wavelength λ for brevity)

$$\text{rs} = \left(0.084 + 0.17\frac{b_b}{a+b_b}\right)\frac{b_b}{a+b_b}$$

$$\left\{1 - \exp\left[-\left(\frac{a+b_b}{\cos(\theta_\omega)} + 1.03\,(a+b_b)\sqrt{1+2.4\frac{b_b}{a+b_b}}\right)H\right]\right\}$$

$$+ \frac{\rho}{\pi}\exp\left[-\left(\frac{a+b_b}{\cos(\theta_\omega)} + 1.04\,(a+b_b)\sqrt{1+5.4\frac{b_b}{a+b_b}}\right)H\right]. \tag{2}$$

The total absorption coefficient is described as the sum of chlorophyll-a (a_ϕ), colored dissolved organic matter (CDOM) (a_g) and pure water (a_ω)

$$a = a_\omega + a_\phi + a_g \tag{3}$$

where a_ω is a constant that is taken from the literature [37]. a_ϕ is defined as follows:

$$a_\phi(\lambda) = [a_0(\lambda) + a_1(\lambda)\,lnP]\,P \tag{4}$$

where the parameters $a_0(\lambda)$ and $a_1(\lambda)$ are taken from the literature [38]; and P is the absorption coefficient of phytoplankton at 440 nm. Spectral $a_g(\lambda)$ is expressed as follows:

$$a_g(\lambda) = G\exp\left[-S\,(\lambda - 440)\right] \tag{5}$$

with the exponent constant S is taken as 0.0166. G is the absorption coefficient of CDOM at 440 nm.

The total backscattering coefficient b_b is described as the sum of pure water b_{bw} and particles b_{bp}:

$$b_b = b_{bw} + b_{bp}. \tag{6}$$

The spectral $b_{bp}(\lambda)$ is expressed as follows:

$$b_{bp}(\lambda) = X\left(\frac{400}{\lambda}\right)^Y \tag{7}$$

where X is a combination of the particle backscattering coefficient at 400 nm, view angle and sea state; and Y is an empirical parameter with a value set to 0.681.

Only one endmember was used to present the reflectance of the substrate in every pixel. Then, the reflectance of the substrate was modeled as follows [23]:

$$\rho = B\rho_{\text{sand}} \tag{8}$$

where ρ_{sand} is the normalized bottom spectral shape of sand, and B is the amplitude of the bottom spectral shape at 550 nm. Therefore, the subsurface remote sensing reflectance of optically shallow water is expressed as a function with five parameters:

$$\text{rs} = f\,(X, P, G, H, B; \lambda). \tag{9}$$

The equivalent remote sensing reflectance at the WV2 or L8 bands is calculated by the following approximation:

$$R_{\text{rs}}^{\text{Sensor}}(\text{Band}_i) \approx \frac{\int_{400}^{900}\text{rs}(\lambda)\,F_{\text{Band}_i}^{\text{Sensor}}(\lambda)\,d\lambda}{\int_{400}^{900}F_{\text{Band}_i}^{\text{Sensor}}(\lambda)\,d\lambda} \tag{10}$$

TABLE II
PARAMETERS ANALYZED IN THE SENSITIVITY ANALYSIS

Symbol	Description	Range of uniform pdf
X	Combines the particle backscattering coefficient, viewing-angle information, and sea state	(0.0005914,0.001797)
P	Phytoplankton absorption coefficient at 440 nm	(0.00566, 0.021)
G	Total absorption coefficient of gelbstoff and detritus at 440 nm	(0.00644,0.0286857)
H	Water depth	(0,1), (1,2), …, (28,29), (29,30)
B	Bottom albedo value at 550 nm	(0.01,0.6)

where $F_{\text{Band}_i}^{\text{Sensor}}(\lambda)$ is the spectral response function of WV2 or L8 at Band_i, which Band_i is the band name of the sensor.

The reflectance of optically shallow water was expressed as a function of X, P, G, H, and B by the semianalytical model. The specific space of these five parameters was analyzed according to Table II. To match the water properties of the study area, satellite-derived inherent optical properties (IOPs) for adjacent optically deep waters [yellow rectangle in Fig. 2(a)] were derived. NASA MODIS monthly average data (4 km pixels) of absorption due to gelbstoff and detritus ($a_g(\lambda)$), the concentration of phytoplankton (C_ϕ) and backscattering due to particles b_{bp} from the Garver–Siegel–Maritorena (GSM) model [39] from July 2012 to August 2019 were downloaded from the GlobColor site.[2] The median value of pixel drops in the yellow rectangle in Fig. 2(a) was calculated. Absorption due to phytoplankton at 440 nm was calculated as follows:

$$P = C_\phi A\,(440)\,C_\phi^{-B(440)} \tag{11}$$

where $A(440)$ and $B(440)$ are 0.0403 and 0.332, respectively [40]. The sampling ranges of three IOPs were obtained from statistics of the time series of X, P, and G. We focus on the variation in amplitude of the bottom reflectance, rather than the shape of the bottom reflectance; the normalized shape of the sand reflectance was used, and the range of B was set to values between 0 and 0.6 [see Fig. 10(a)] The total range of the water depth is divided into 30 parts with a step size of 1 m. Finally, there are 30 groups of parameter space in total (see Table II).

2) Latin-Hypercube-One-Factor-at-a-Time Method: This method subdivides the distribution of each parameter into N strata with a probability of occurrence equal to 1/N. Random values of the parameters are generated such that for each of the five parameters, each interval is sampled only once. Then, we obtain N samples, namely N Latin Hypercube points. N is empirically set to 6 (based on our test, the number of strata does not influence the result).

The method operates by loops. Each loop starts with a Latin Hypercube point. Around each Latin Hypercube point, a partial effect $S_{i,j}$ for each parameter is calculated as follows (in

---

[2]Online. [Available]: http://hermes.acri.fr/.

percentage) [35]:

$$S_{i,j} = \left| \frac{100 * \left(\frac{f(X,P,G,H(1+\Delta f_i),B) - f(X,P,G,H,B)}{f(X,P,G,H(1+\Delta f_i),B) + f(X,P,G,H,B)} \right)}{\Delta f_i} \right| \quad (12)$$

where $f(X, P, G, H, B)$ refers to the forward model of optically shallow waters (9); note that wavelength λ is omitted for brevity), Δf_i is the fraction by which the parameter is changed (a predefined constant: 0.1) and j refers to an LH point. In (12), the parameter was increased with the fraction Δf_i, but it can also be decreased since the sign of the change is randomly defined. Therefore, a loop requires PC 1 runs. The final effect is calculated by averaging the partial effects of each loop and is normalized to a range of 0-1.0.

E. Log-Ratio Method

The LRM developed by [7] is expressed as follows:

$$H = m_0 \frac{\ln \left(qR_{\rm rs} \left({\rm Band}_1 \right) \right)}{\ln \left(qR_{\rm rs} \left({\rm Band}_2 \right) \right)} + m_1 \quad (13)$$

where m_1 and m_0 are empirical parameters. H is the water depth. q is a constant value. Traditionally, ${\rm Band}_1$ and ${\rm Band}_2$ correspond to the blue and green band respectively. If *in situ* bathymetry data are available, then the empirical parameters can be tuned with *in situ* bathymetry data. The band ratio is defined as follows:

$$\text{Band Ratio} = \frac{\ln \left(qR_{\rm rs} \left({\rm Band}_1 \right) \right)}{\ln \left(qR_{\rm rs} \left({\rm Band}_2 \right) \right)} \quad (14)$$

F. Unmixing-Based Multispectral Optimization Process Exemplar (UMOPE) Method

A robust linear mixing model was used to address the mixing phenomenon in coral reefs. In this case, the albedo of the substratum was modeled as follows [9], [41]:

$$\rho \left(\lambda \right) = B_1 \rho_1 \left(\lambda \right) + B_2 \rho_2 \left(\lambda \right) + B_3 \rho_3 \left(\lambda \right) \quad (15)$$

with

$$\min < \sum_{i=1}^{3} B_i < \max \quad (16)$$

where ρ_i represents the reflectance of sand, coral and seagrass [see Fig. 10(a)]. B_i is a combination of the proportions of each endmember and the reflectance scaling factor for the three endmembers. The two thresholds were empirically set to min = 0.1 and max = 1.2 [9].

Thus, $R_{\rm rs}$ is expressed as a function of seven unknown parameters (note that λ is omitted for brevity)

$$rs = f \left(X, P, G, H, B_1, B_2, B_3 \right). \quad (17)$$

The subsurface reflectance (rs) is translated into the reflectance at the water surface (R_{rs}) by the following equation [23]:

$$R_{\rm rs} = \frac{0.5 rs}{1 - 1.5 rs}. \quad (18)$$

The cost function bellow was built via spectral matching

$$\text{obj} = \sqrt{\frac{\left(\Lambda_{B_1}^{B_n} \left(R_{\rm rs\_model} \left({\rm Band}_i \right) - R_{\rm rs\_true} \left({\rm Band}_i \right) \right)^2 \right)}{\Lambda_{B_1}^{B_n} \left(R_{\rm rs\_true} \left({\rm Band}_i \right) \right)}}$$

$$(19)$$

where $R_{\rm rs\_model}$ is modeled by (17) and (18). $R_{\rm rs\_true}$ is the true remote sensing reflectance obtained from atmospherically corrected imagery. The water depth is estimated by minimizing the cost function by the "Fmincon" function in the MATLAB optimization toolbox. The ranges for X, P, and G were taken from Table II.

G. Applicable Depth Range Analysis

Legleiter and Roberts [42] developed the optimal band ratio analysis to identify the optimal band ratio for the whole depth range. Based on optimal band ratio analysis, we develop ADRA to not only identify the optimal band ratio for depth ranges, but also to identify the depth range to be used for a specific band ratio. We call the depth range to be most appropriately used for a specific band ratio as the applicable depth range. The coefficient of determination (R^2) in a regression of water depth against band ratio is an index of a band combination's fitness to a specific depth range [42]. This index was adopted in the ADRA.

When *in situ* bathymetry data are available, these data are used to conduct the ADRA. If the *in situ* bathymetry data are absent, we adopted the solution provided by Liu *et al.* [17] to obtain bathymetry data. Water depths estimated by the UMOPE method were used as the measured water depths to conduct the ADRA. We assumed that the applicable depth range of each band ratio only varies on the upper limit, and the lower limit is fixed as 0.

In our previous study, we found that the slope of the linear regression line increases with the depth range [17]. In addition to linear regression, logarithmic regression was carried out between the band ratio and water depth

$$H = m_0 \cdot ln \left(\frac{\ln \left(qR_{\rm rs} \left({\rm Band}_1 \right) \right)}{\ln \left(qR_{\rm rs} \left({\rm Band}_2 \right) \right)} \right) + m_1. \quad (20)$$

To explain the reason to use logarithmic regression, we simulated the water-leaving reflectance with the forward model. The median values of the ranges of X, P, and G in Table II and H ranged from 0.2 to 40 m, with a step of 0.2 m, and were plugged into the forward model. Reflectance spectra of sand and coral reef were included in the forward model. The band-set of WV2 was also chosen as an example.

Taken together, ADRA was implemented with the following steps.

1) The lower limit of the depth range is set as 0 m. The temporary upper limit of the depth range increases from 2 to 20 m with a step of 1 m.
2) Each temporary upper limit and the lower limit form the temporary optimal range of each band ratio. A total of 450 pixels were sampled within the temporary applicable range. The correlation coefficient (R^2) between the band ratio and water depth was calculated. We repeated the procedure 100 times for each temporarily applicable depth

range and obtained 100 values of R^2. Then, the average value ($\epsilon(R^2)$) of R^2 was calculated.

3) Scatterplots between the upper limit of the depth range and $\epsilon(R^2)$ were plotted for each band ratio. We selected the depth range that has the largest value of R^2 as the applicable depth range of each band ratio.

H. Adaptive Blended Algorithm Approach

1) Determining Subalgorithms Automatically: The ABAA is composed of several subalgorithms. However, not all the band ratios can be used as the sub-algorithms for the ABAA because some band ratios have the same applicable depth range. From the perspective of depth range, each depth range has an optimal band ratio. The optimal band ratio for each depth range can also be derived from ADRA. In that way, a strict selection criterion for subalgorithms (LRM with optimal band ratios) in the ABAA was formed: If a band ratio has an applicable depth range, and the band ratio is the optimal band ratio of the depth range, then the LRM with the band ratio is selected as a subalgorithm for the ABAA. Consequently, sub-algorithms sharing the same applicable depth range do not exist.

However, some subalgorithms may share similar applicable depth ranges (not the same), and there is a need to filter the sub-algorithms for conveniently merging bathymetry results from subalgorithms. First, subalgorithms were ranked in descending order of applicable depth range. Second, from top to bottom starting at the subalgorithm that has the second largest applicable depth range, each target subalgorithm is compared with its closest upper-level sub-algorithm (upper-level means larger applicable depth range here). Then, if the applicable depth range of the target subalgorithm is 2 m narrower than that of its closest upper-level subalgorithm, the target sub-algorithm is selected as the final subalgorithm. Finally, the subalgorithms for the ABAA are determined.

2) Merging Bathymetry Results from Subalgorithms: The remaining problem of the ABAA involves seamlessly combining bathymetry results of optimal band ratios. A merging method described in [25] was adopted, and the transition buffer is empirically set as 2 m:

$$H_{\text{ABAA}} = \begin{cases} H_i & if\ H_1 < H_i^U - 1 \\ \alpha \cdot H_i + \beta \cdot H_{i-1} & if\ H_i^U - 1 < H_1 < H_i^U + 1 \\ H_{i-1} & if\ H_1 > H_i^U + 1 \end{cases}$$
(21)

where H_1 is the water depth estimated by the subalgorithm that has the largest applicable depth range. If the number of subalgorithms is more than 2, then the value of H_1 was updated after each merge operation. H_{i-1} and H_i represent the water depth estimated by the upper-level subalgorithm and lower-level sub-algorithm, respectively. H_i^U is the upper limit of the applicable depth range of the lower-level subalgorithm. α and β are defined as follows:

$$\alpha = \left(H_1 - H_i^U + 1\right)/2$$
(22)

$$\beta = \left(H_i^U + 1 - H_1\right)/2.$$
(23)

I. Evaluation of the Method

The new method ABAA was compared with its subalgorithms and UMOPE.

Before assessing the bathymetric results, a tidal correction was applied to the estimated and measured depths using the following equation:

$$H\prime = H(t) + \triangle H(t)$$
(24)

where $\triangle H(t)$ is the difference between the vertical reference datum and the tidal height at time t. Tidal data were collected from published tide tables, which were edited by the National Marine Data and Information Service, China.

The root-mean-square error (RMSE) of the estimated depth within 1-m-depth bins was calculated to assess the accuracy of the bathymetry method. The RMSE is defined as follows:

$$\text{RMSE} = \sqrt{\frac{1}{m}\sum_{i=1}^{m}\left(H\prime - H\right)^2}$$
(25)

where $H\prime$ and H are the corrected estimated depth and measured depth, respectively; and m is the number of verification points for different depth ranges.

III. Results

A. Results of the Sensitivity Analysis

Fig. 3 shows the results from the global sensitivity analysis of the semianalytical model. In the blue and coastal band, from 0 to 30 m, the variation in water-leaving reflectance is first dominated by bottom reflectance and is then dominated by water optical parameters. The results in the blue and coastal band indicate that the variation in water depth is not important in explaining the variation in water-leaving reflectance, compared with other parameters. In the green band, water depth has the strongest influence on the variation in water-leaving reflectance from 10 to 20 m, accounting for 40% of the variance. For water depths ranging from 0 to 10 m, the variation in water-leaving reflectance is dominated by bottom reflectance, accounting for 80%–40% of the variance. After 20 m, the backscattering coefficient (X) dominates the variation in water-leaving reflectance, accounting for more than 40% of the variance. In the green band, the variation in water depth is still the second largest contributor to the variation in water-leaving reflectance from 0 to 10 m and after 20 m. In the yellow, red and red-edge band, the variation in water depth dominates the variation in water-leaving reflectance from 1 to 11 m, from 0 to 7 m and from 0 to 3 m, respectively. After reaching the upper limit of those ranges, X dominates the reflectance, which accounts for more than 75% of the variance. With the increase in wavelength at the band, the water depth accounts for more of the variance in the water-leaving reflectance within different depth ranges. We also find that, with the increase in water depth, the contribution from the water depth first increases and then decreases in all bands.

In short, the results from the sensitivity analysis indicate that the water-leaving reflectances at the green, yellow, red, and red-edge band are sensitive to the variance in water depth within specific depth ranges, and the water-leaving reflectances
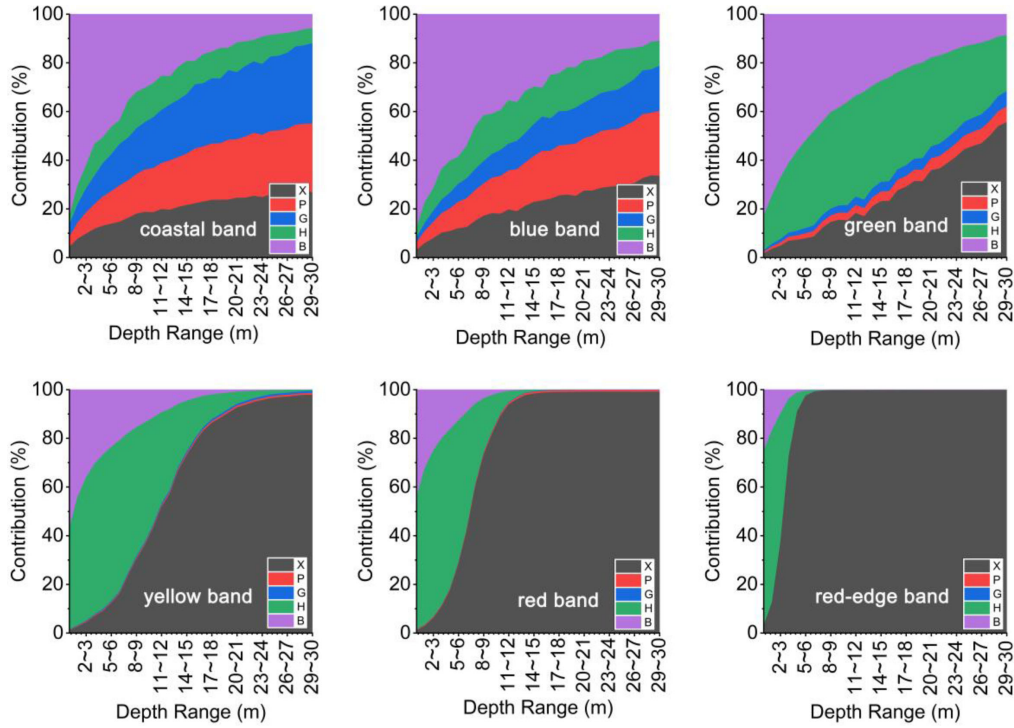
Fig. 3.   Specific range sensitivity analysis of six visible bands of WV2 with the semianalytical optically shallow water model. Here, the *y* axes represent the contribution from *X, P, G, H,* and *B* to the variance in water-leaving reflectance.
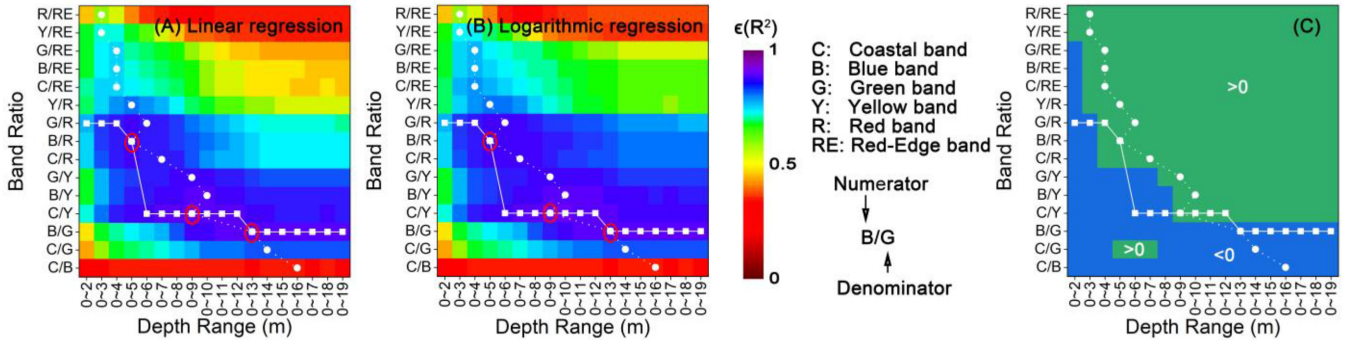

Fig. 4.   A sample of ADRA matrices for different band ratios (WV2 image acquired in 2011). (a) ADRA matrices for $\epsilon(R^2)_{\text{linear regression}}$. (b) ADRA matrices for $\epsilon(R^2)_{\text{logarithmic regression}}$. (c) Matrices for $\epsilon(R^2)_{\text{logarithmic regression}} - \epsilon(R^2)_{\text{linear regression}}$. White spheres connected by dotted line form the applicable depth range of each band ratio. White squares connected by solid line form the optimal band ratio for each depth range. Red circles enclose the applicable depth range for alternative band ratios.

at the coastal and blue band are not sensitive to the variance in water depth. The band ratio with the coastal or blue band in the numerator and green band, yellow band, red, or red-edge band in the denominator meet the band selection criteria of the LRM within specific depth ranges. More importantly, with the increase of water depth, the sensitive wavelength band in the water-leaving reflectance for the water depth varies from the longer wavelength band to the shorter wavelength band.

B. Results of ADRA

ADRA were applied to three WV2 images and three L8 images. A sample of ADRA matrices is summarized in Fig. 4

(WV2 image acquired in 2011). The sample of ADRA was conducted with *in situ* bathymetry data. An important finding of ADRA is that there is a global maximum for the $\epsilon(R^2)$ in Fig. 4. Then, the maximum value can be easily automatically recognized as the upper limit of the applicable depth range from the ADRA matrices by comparison. Applicable depth ranges for each band ratio are shown with white spheres connected by dotted lines in Fig. 4(a)–(c). When the band in the denominator of the band ratio varies from the longer wavelength band to the shorter wavelength band, the upper limit of the applicable depth range increases. Band ratios with the same band in the denominator share similar applicable depth ranges. Furthermore, the applicable depth range of logarithmic regression is almost the

TABLE III
INFORMATION ON THE SUBALGORITHMS FOR THE ABAA

	WorldView-2	Sub-algorithm information			Landsat-8	Sub-algorithm information		
	Imaging Time	Band Ratios	Applicable depth range (m)	Regression Method	Data ID	Band Ratios	Applicable depth range (m)	Regression Method
With in-situ data	2011-01-05	B/G	0~13	Linear	LC8122048201 4176LGN00	B/G	0~15	Linear
		C/Y	0~9	Logarithmic		G/R	0~5	Logarithmic
		B/R	0~5	Logarithmic	LC8122048201 6166LGN00	B/G	0~18	Linear
	2015-10-25	B/G	0~12	Linear		C/R	0~7	Logarithmic
		C/Y	0~7	Logarithmic		G/R	0~4	Logarithmic
	2019-07-15	B/G	0~15	Linear	LC8122048201 7200LGN00	B/G	0~17	Linear
		C/Y	0~8	Logarithmic		B/R	0~7	Logarithmic
		C/R	0~4	Logarithmic				
Without in-situ data	2011-01-05	B/G	0~4	Linear	LC8122048201 4176LGN00	B/G	0~15	Linear
		C/Y	0~6	Logarithmic		G/R	0~5	Logarithmic
	2015-10-25	B/G	0~5	Linear	LC8122048201 6166LGN00	B/G	0~19	Linear
		C/Y	0~6	Logarithmic		C/R	0~7	Logarithmic
	2019-07-15	B/G	0~4	Linear	LC8122048201 7200LGN00	B/G	0~17	Linear
		C/Y	0~8	Logarithmic		C/R	0~8	Logarithmic

*C, B, G, Y and R are short for Coastal, Blue, Green, Yellow and Red band, respectively.

same as that of linear regression, and it is easy to obtain the best regression method for a band ratio by comparing the R^2 within its applicable depth range [see Fig. 4(c)]. In Fig. 4(c), the best regression method of optimal band ratios is nearly dominated by bands in the denominator. When the band ratio includes the yellow or red band in the denominator, the best regression method is a logarithmic regression [green color in Fig. 4(c)]. When the band ratio includes the green band in the denominator, the best regression method is more likely to be a linear regression [blue color in Fig. 4(c)].

The optimal band ratio for each depth range is shown with white squares connected by solid line in Fig. 4(a) and (b). With the increase of depth range, the band in the denominator of the optimal band ratio varies from the longer wavelength band to the shorter wavelength band.

Based on the selection criterion of sub-algorithms (LRM with optimal band ratios) for the ABAA, the intersection points of the white dotted line and white solid line indicate the information of subalgorithms, including the optimal band ratios and corresponding applicable depth ranges. The information of subalgorithms for the ABAA is given in Table III.

When the *in situ* bathymetry data were used to conduct ADRA, WV2 images acquired in 2011 and 2019 and an L8 image acquired in 2016 have three sub-algorithms. A WV2 image acquired in 2015 and two L8 images acquired in 2011 and 2017 have two subalgorithms. The LRM(B/G) usually has the largest applicable depth. Except for the L8 image that was acquired in 2011, when the band in the denominator of the band ratio varies from the longer wavelength band to the shorter wavelength band, the upper limit of the applicable depth range increases.

When the *in situ* bathymetry data are absent, only two subalgorithms can be determined for all images. The applicable depth range for the LRM with the yellow or red band in the denominator is similar to those derived with *in situ* data. For WV2 images, only the LRM with the yellow and green band in the denominator can be determined. The applicable depth range of the LRM(B/G) is unusually small for a WV2 image. Thus, we artificially set the LRM(B/G) as a sub-algorithm of the ABAA and set the applicable depth range the LRM(B/G) as 20 m. Note that the threshold value may change due to different IOPs.

C. Bathymetry Result With In Situ Bathymetry Data

Density scatter plots between the estimated depth and the LiDAR or sonar measured depth are shown in Fig. 5. The blue arrows point to the upper limit of the applicable depth range of each sub-algorithm. As a whole, the ABAA performs better than the subalgorithm (LRM with a single band ratio) with more compact scatters around the diagonal line. Among those subalgorithms, the LRM(B/G) performs the best in the whole depth range of the optically shallow region without significant bias from the diagonal (the first column in Fig. 5). The LRM with the yellow or red band in the denominator performs better than the LRM(B/G) within their applicable depth ranges with points more closely distributed to the 1:1 line. However, the LRM with the yellow or red band in the denominator shows significant biases after a specific depth, which are larger than the upper limit of their applicable depth ranges.

Fig. 6 shows the RMSE of derived water depths within 1-m-depth bins. The histograms indicate the number of counts
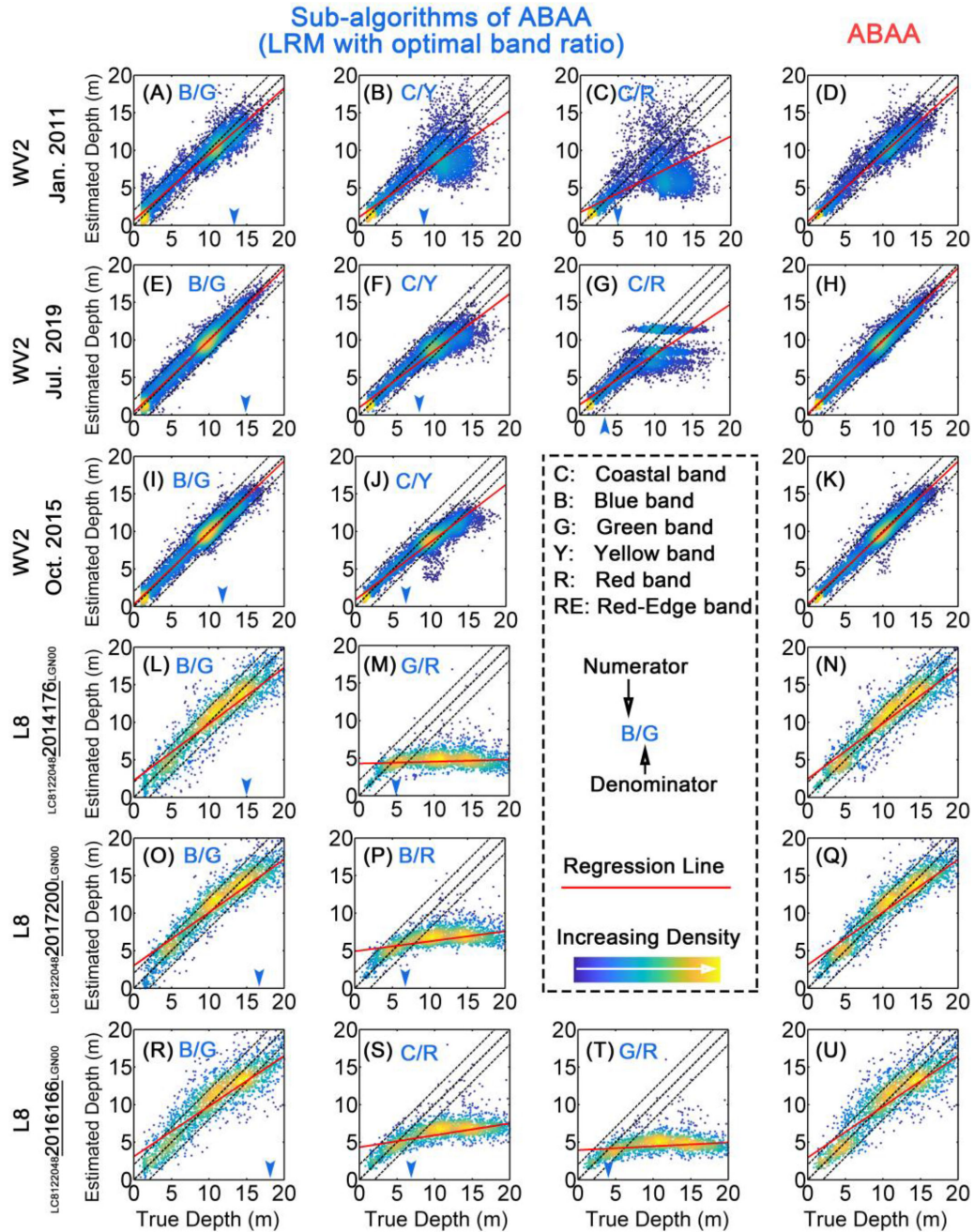
Fig. 5.   Density scatter plots of estimated depth from WV2 images and L8 images versus true depth (LiDAR data and sonar data). The red solid line represents the regression line. Each line represents the scatter plots of an image. The blue arrows point to the upper limit of the applicable depth range of each sub-algorithm. The first three columns represent the scatter plots of subalgorithms. The fourth column represents the scatter plots of ABAA.

within each bin. The arrows point to the upper limit of the applicable depth range of each subalgorithm. The LRM with the yellow or red band in the denominator performs better than the LRM(B/G) within their applicable depth ranges with a lower value of RMSE. For WV2 images, the LRM with the red band in the denominator performs better than the LRM with the yellow band in the denominator. An unexpected finding is that the LRM(C/R) performs better than the LRM(G/R) within the applicable depth range of the LRM(C/R) [see Fig. 6(e)] even though they share the same band in the denominator. The ABAA

combines the advantages of subalgorithms. Compared with the LRM(B/G), the ABAA increases the accuracy of the estimated water depth for waters shallower than 6 m. When the water is shallower than 6 m, the RMSE of the ABAA varies from 0.31 to 0.94 m for WV2 data and from 0.25 to 1.42 m for L8 data.

Fig. 7 shows the seamless bathymetric maps derived by the ABAA from three WV2 images and three L8 images. Large areas of the coral reef are shallower than 6 m, indicating that it is important to increase the accuracy of the estimated water depth for these shallow regions.
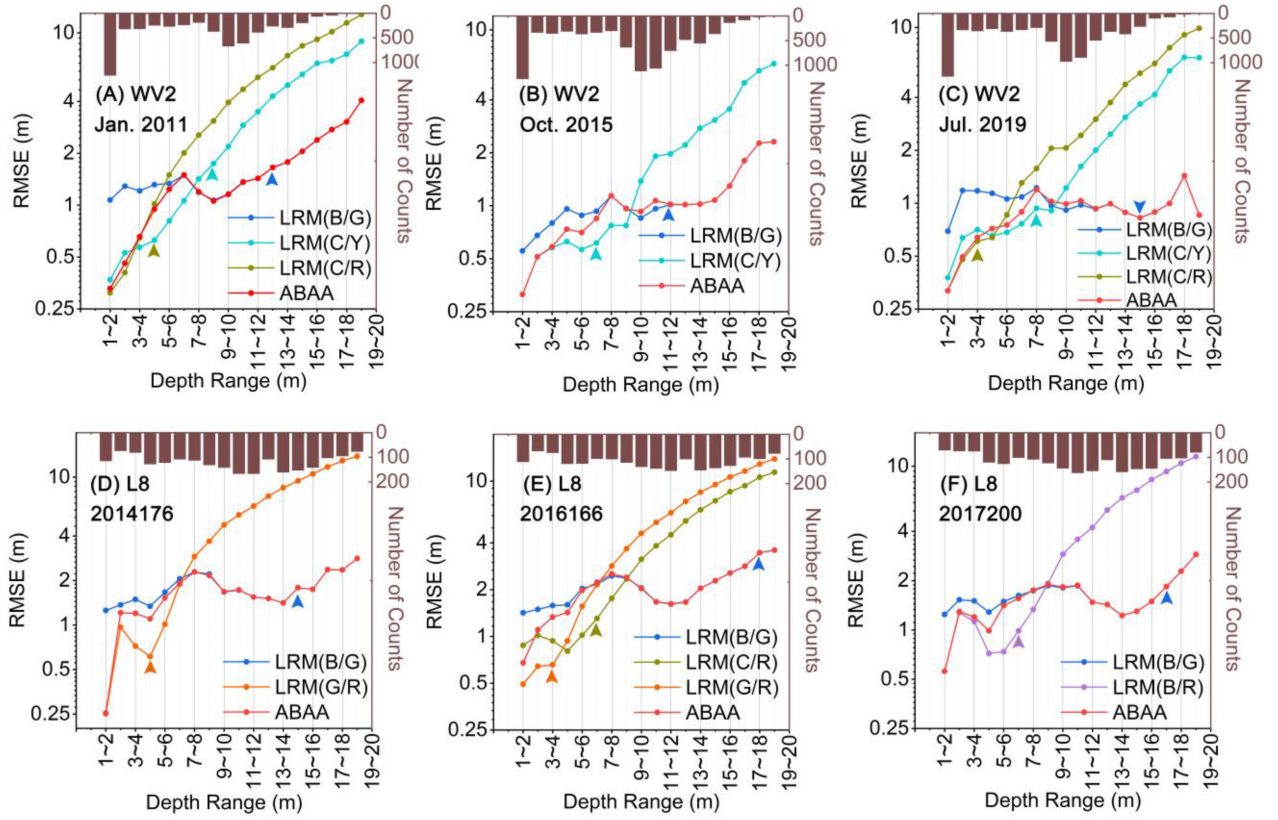
Fig. 6. RMSE between estimated depth and measured depth at different ranges when the *in situ* bathymetry data are available. The arrows point to the upper limit of the applicable depth range of each sub-algorithm. The histograms represent the number of counts within each bin.
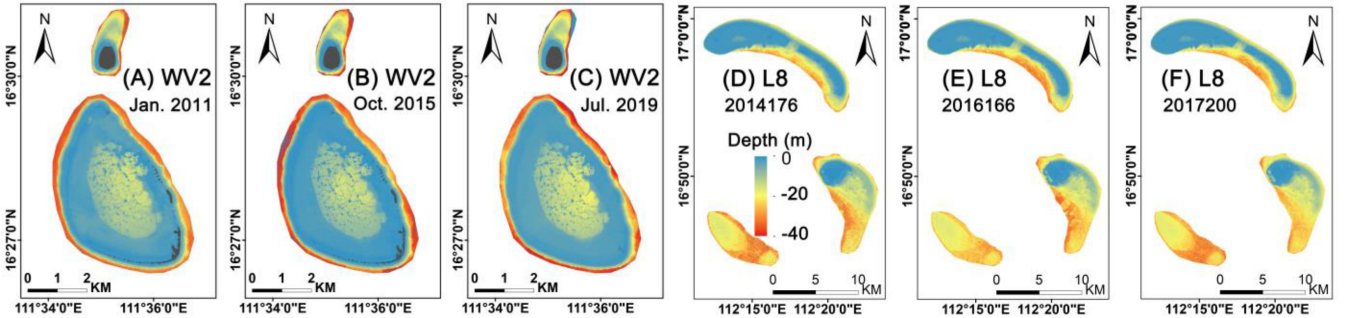

Fig. 7. (a)–(c) Bathymetric map derived from ABAA with a 2-m (WV2) resolution for Ganquan Dao. (d)–(f) Bathymetric map derived from ABAA with a 30-m resolution (L8) for Qilian Yu and Yongxing Dao. Black color represents land or invalid data. Note that the missing area due to clouds in (e) was repaired by (f).

D. Bathymetry Results Without In Situ Bathymetry Data

When the *in situ* bathymetry data are absent, scatter plots between the estimated depth and the LiDAR or sonar measured depth are shown in the first line of Fig. 8. With the increase of water depth, the ABAA and LRM(B/G) show a similar trend to underestimate or overestimate water depth similar to UMOPE. Compared with the UMOPE method, the ABAA and LRM(B/G) perform better with more compact scatters after approximately 8 m. The LRM with the yellow or red band in the denominator performs better than the LRM(B/G) within their applicable depth ranges with more compact scatters. However, the LRM(B/G) performs better than the LRM with the yellow or red band in the denominator after a specific depth. Compared with those subalgorithms, the ABAA performs better by taking advantage of sub-algorithms.

Fig. 9 shows the RMSE of derived water depths within 1-m-depth bins. Except for Fig. 9(d), the comparison results for the other images are almost consistent. For water depth ranges from 1 to 6 m, the accuracy of the LRM(B/G) is not only lower than that of the LRM with the red or yellow band in the denominator but also lower than that of UMOPE. For depth ranges from 1 to 3
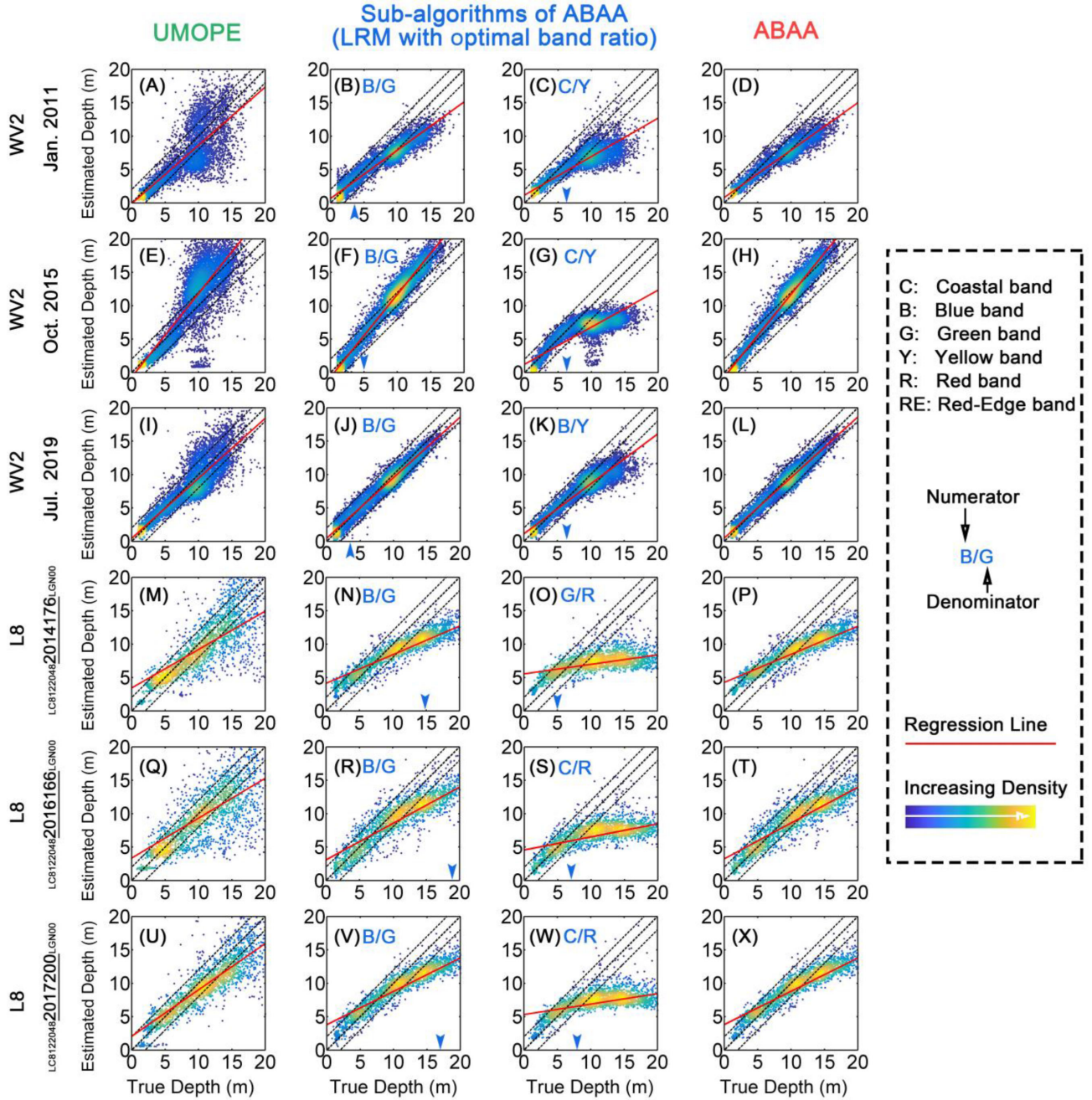
Fig. 8. Density scatter plots of estimated depth from WV2 images and L8 images versus true depth (LiDAR data and sonar data). The red solid line represents the regression line. Each line represents the scatter plots of an image. The first column represents the scatter plots of UMOPE. The second and third columns represent the scatter plots of subalgorithms. The blue arrows point to the upper limit of the applicable depth range of each subalgorithm. The fourth column represents the scatter plots of ABAA.

m, the accuracy of UMOPE is higher than that of the LRM with different band ratios. In Fig. 9(d) and (e), the accuracy of the UMOPE is higher than that of LRM with different band ratios within a wider depth range (1–5 m). Even though the accuracy of the ABAA is lower than that of UMOPE for depth ranges from 1 to 3 m or from 1 to 5 m, the ABAA combines the advantages of subalgorithms with a lower value of RMSE than that of UMOPE for water depths deeper than 3 or 5 m.

IV. DISCUSSION

A. Relationship Between Sensitivity Analysis and Bathymetry Inversion Strategy

Conducting sensitivity analysis helps in understanding the mechanism of constructing the inversion strategy. Under the assumption that water optical properties are highly similar across the studied regions, the result of the sensitivity analysis in
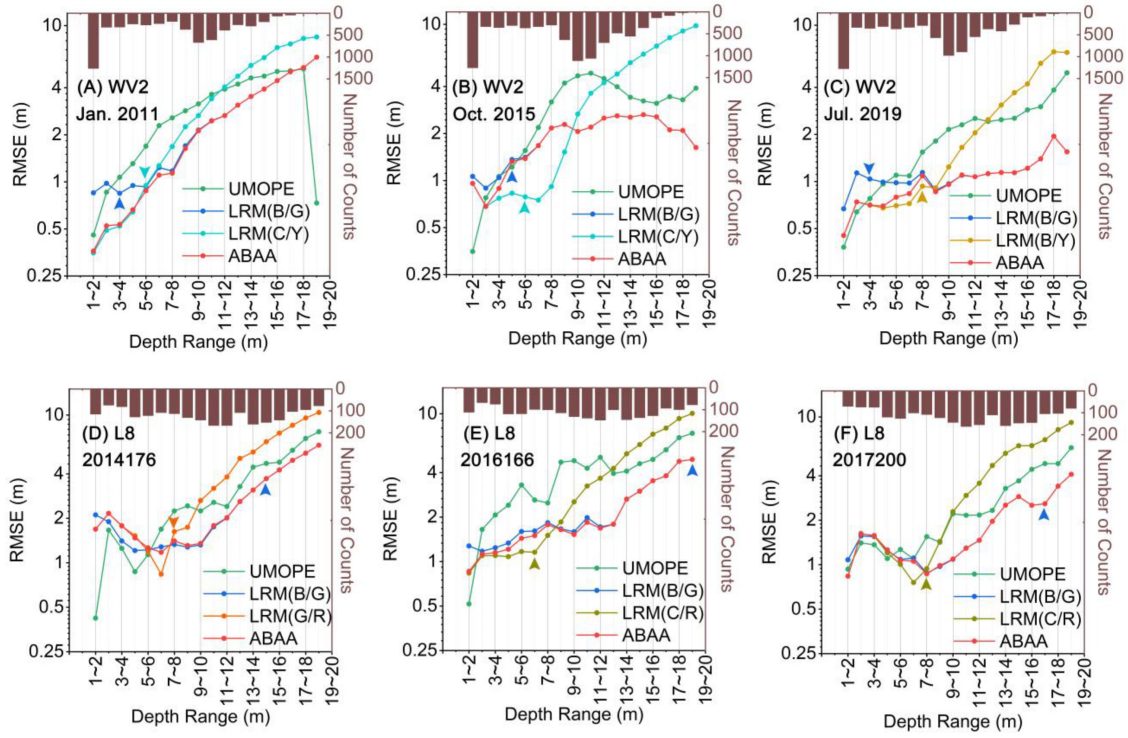
Fig. 9. RMSE between estimated depth and measured depth at different ranges when the *in situ* bathymetry data are absent. The arrows point to the upper limit of the applicable depth range of each subalgorithm. The histograms represent the number of counts within each bin.

the green band has supported the use of reflectance data at the green band for a wide range of water depths in previous studies [13]–[19]. With the decrease of water depth, the sensitive wavelength band in water-leaving reflectance for the water depth varies from the shorter wavelength band to the longer wavelength band (from the green band to the red-edge band). Bathymetry results echo the results of the sensitivity analysis and show that the LRM with the most sensitive band in the denominator always performs the best. For example, when the water depth is shallower than approximately 5 m, the depth in the red band contributes more than that in the yellow or green band to the variance of water-leaving reflectance. Then, the LRM with the red band in the denominator performs better than the LRM with the green or yellow band in the denominator. The ABAA takes advantage of different band ratios, performing better than the LRM with a single band ratio.

In addition to the selection of the band ratio, determining the applicable depth range of each band ratio is also motivated by the results of sensitivity analysis. We artificially set the lower limit of the applicable depth range for each band ratio as 0 m because the results from the sensitivity analysis show that water depth is the largest or second-largest contributor to water-leaving reflectance within the depth range whose lower limit is near 0 m, and becomes one of the smallest contributors to water-leaving reflectance when the water depth is deeper than a specific value.

In short, the sensitivity analysis ensured the mechanism of ABAA.

B. Choice Between Linear Regression and Logarithmic Regression

Our results indicate that when the band ratio includes the yellow or red band in the denominator, the best regression method is the logarithmic regression. When the band ratio includes the green band in the denominator, the best regression method is more likely to be linear regression.

Fig. 10(B) indicates that the simulated reflectance and water depth exhibit a logarithmic relation. The natural logarithm of the simulated reflectance ($\ln(\mathrm{rs})$) is linear with water depth in bands with shorter wavelengths, such as the coastal band, blue, and green band [see Fig. 10(c)]. The result can further explain why the LRM with the blue and green band performs well with the linear regression. At bands with a longer wavelength, such as the yellow, red and red-edge band, $\ln(\mathrm{rs})$ and water depth still exhibit logarithmic relationships within specific depth ranges [see Fig. 10(c)]. Then, there is a logarithmic relationship between the ratio between the natural logarithm of a band with a shorter wavelength and the natural logarithm of a band with a longer wavelength and water depth, and the ratio between the natural logarithms of two bands with a short wavelength is linear with the water depth [see Fig. 10(d)].

Furthermore, the relationship between water-leaving reflectance and water depth is the primary cause. (2) is simplified into the following equation:

$$\mathrm{rs} = \left(\frac{\rho}{\pi} - \mathrm{rs}_{\mathrm{deep}} \right) \exp\left(-gH \right) + \mathrm{rs}_{\mathrm{deep}} \qquad (26)$$
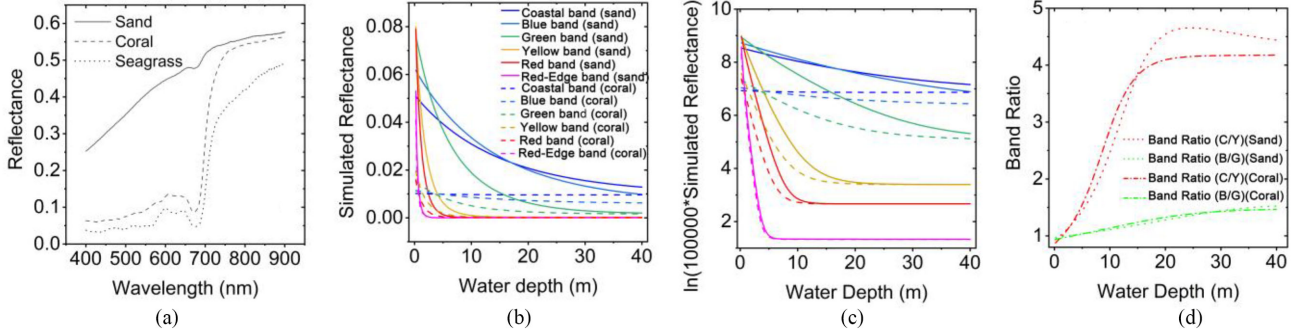
Fig. 10.   (a) Reflectance of sand, coral, and seagrass [9]. (b)Value of simulated reflectance of WV2 as a function of water depth. (c) Natural logarithm value of simulated reflectance of WV2 as a function of water depth. (d) Band ratio as a function of water depth. (b) and (c) share the same legend.

where g is a function of the diffuse attenuation coefficients for both downwelling and upwelling signals. The natural logarithm was taken on both sides of (26)

$$\ln\left(\mathrm{rs}\right) = \ln\left[\left(\frac{\rho}{\pi} - \mathrm{rs_{deep}}\right)\exp\left(-gH\right) + \mathrm{rs_{deep}}\right]. \quad (27)$$

If $\mathrm{rs_{deep}}$ is equal to 0, $\ln(\mathrm{rs})$ is obviously linear with the water depth (H) regardless of the value of g. Then, the band ratio is likely linearly dependent on the water depth. In fact, $\mathrm{rs_{deep}}$ is greater than zero, and the relationship between $\ln(\mathrm{rs})$ and water depth becomes complicated. Based on our test (not shown here), if the g value in (27) is large (corresponding to strong diffuse attenuation in the yellow or red band), $\ln(\mathrm{rs})$ shows a logarithmic correlation with water depth, regardless of the value of $\mathrm{rs_{deep}}$. Even though $\mathrm{rs_{deep}}$ can be calculated first [29], [43], the value of $\mathrm{rs_{deep}}$ is not error-free. Then, $\ln(\mathrm{rs})$ still shows a logarithmic correlation with water depth within a specific depth range in the red band. In short, the logarithmic relation between $\ln(\mathrm{rs})$ and water depth was caused by the strong attenuation coefficient and the existence of optically deep water column reflectance in (26). Taken together, when we use bands with strong diffuse attenuation, the logarithmic regression should be taken into consideration.

C. Factors Influencing the Selection of Optimal Band Ratios

Among those three WV2 images, the WV2 image acquired in 2015 obtained only two optimal band ratios [see Fig. 6(b) and (e)], namely a band ratio with the green band and a band ratio with the yellow band in the denominator. The phenomenon was mainly caused by the signal-to-noise ratio (SNR) and interleave between two adjacent bands.

The red or red-edge band, which has a low value due to the strong absorption of water, usually has a low SNR. Thus, more pixels with abnormal values will be involved in ADRA and the coefficient of determination (R^2) in a regression of water depth against band ratio was reduced. Consequently, the advantage of the red or red-edge band is not reflected in the coefficient of determination (R^2) in a regression of water depth against the band ratio. Moreover, the advantage of the red or red-edge band is also likely covered by adjacent bands with shorter wavelengths. For example, the interval between the red and green band is wider than that between the red and yellow band. Due to the lack of

a yellow band between the red and green band, L8 images can always obtain at least two optimal band ratios, namely a band ratio with the green band in the denominator and a band ratio with the red band in the denominator. Thus, two optimal band ratios can be easily selected from other high spatial resolution images that do not have yellow bands.

From Fig. 10(d), we can observe that different bottom types result in different correlations between the band ratio and water depth. To some extent, ADRA can find the band ratio that is influenced less by the bottom reflectance. Among those three L8 images, the L8 image acquired in 2016 obtained two subalgorithms sharing the same band in the denominator. Nevertheless, we observed that the LRM(G/R) performs better than the LRM(C/R) when water is shallower than 5 m. In other words, bands in the numerator of the LRM also influence the applicable depth range and bathymetry results. Bottom reflectance in the green band contributes less than that in the costal band to the water-leaving reflectance. Thus, ADRA can find the band ratio that is influenced less by the bottom reflectance. If we can obtain the bottom type first, the method can be further improved. The improvement idea is another topic. A more detailed discussion can be found in the literature [3], [16], [42].

D. Limitation of the ABAA

When the ABAA was applied to the situation where the *in situ* bathymetry data are absent, the applicable depth range of the LRM(B/G) is unusually small for WV2 images. However, the applicable depth range of the LRM with the yellow or red band in the denominator is normal. This is mainly caused by the error introduced by UMOPE. We observed that the accuracy of UMOPE decreases significantly with the increase of water depth. Particularly after 8 m, a large bias of the bathymetry result derived by UMOPE can be observed (the first column in Fig. 8). The phenomenon is not observed from the results of L8, even though L8 has less visible bands. It may be that the SNR of L8 is higher than that of WV2 or the atmospheric correction method of WV2 did not consistently produce sufficiently accurate water reflectance from the shallow region to the deep region. Note that we did not apply the ABAA to the imagery with three visible bands when *in situ* bathymetry data were absent, because the UMOPE method performed poorly in our previous study [17].

The adaptive-look-up table (ALUT) can be used for imagery with three visible bands to estimate water depth [5], [44]. The combination of the ALUT and LRM methods is an alternative solution.

Another limitation of the ABAA is that the information available in all bands influenced by depth is not fully used. To conveniently merge the bathymetry results from subalgorithms, the filtering mechanism of subalgorithms leaves out some band ratios that have similar applicable depth ranges as the subalgorithms. The use of machine learning algorithms may be a good solution to fully use the information available in all the bands influenced by depth.

V. CONCLUSION

In this article, motivated by the results of a global sensitivity analysis showing that the sensitive wavelength in water-leaving reflectance for water depth varies from the longer wavelength band to the shorter wavelength band with increasing water depth, and the variance in water depth can dominate the variance in water-leaving reflectance at the green, yellow, red, and red-edge band within different specific depth ranges, we proposed a blended algorithm approach that can estimate water depth at different water depth ranges with the most sensitive band. Since there are many operational high spatial resolution satellite sensors that have at least three visible bands, the LRM with applicable depth ranges or subalgorithms for the ABAA were selected by our developed ADRA, which can automatically search the applicable depth range for each band ratio. Furthermore, logarithmic regression was taken into consideration due to bands with strong diffuse attenuation, such as the red band.

The ABAA was applied to WV2 data and L8 data of Xisha Qundao. When the *in situ* bathymetry data are available, the verification result shows that the ABAA is outstanding compared with the LRM with the blue and green bands in regions shallower than 6 m (RMSE = 0.31 to 0.94 m for WV2 data, RMSE = 0.25 to 1.42 m for L8 data). Since large areas of optically shallow waters shallower than 6 m on Xisha Qundao can be observed from bathymetric maps derived from WV2 or L8 data, the ABAA demonstrates its superiority. Moreover, the modified ABAA can also work without *in situ* data after incorporating the optimization-based method (UMOPE) developed by Liu *et al.* [9]. When the *in situ* bathymetry data are absent, compared with the LRM with the blue and green bands and UMOPE, the ABAA performs better overall. The major disadvantage of the ABAA is that it cannot be applied to satellite data that have only three visible bands when the *in situ* bathymetry data are absent. In the future, this problem should be resolved.

V. DISCLOSURES

The authors declare no conflicts of interest.

REFERENCES

[1] F. Moberg and C. Folke, "Ecological goods and services of coral reef ecosystems," *Ecol. Econ.*, vol. 29, no. 2, pp. 215–233, May 1999.

[2] J. A. Goodman, S. J. Purkis, and S. R. Phinn, in *Coral Reef Remote Sensing.* Dordrecht, The Netherlands: Springer, 2013.

[3] C. Cahalane, A. Magee, X. Monteys, G. Casal, J. Hanafin, and P. Harris, "A comparison of Landsat 8, rapideye and pleiades products for improving empirical predictions of satellite-derived bathymetry," *Remote Sens. Environ.*, vol. 233, Nov. 2019, Art. no. 111414.

[4] F. Eugenio, J. Marcello, and J. Martin, "High-resolution maps of bathymetry and benthic habitats in shallow-water environments using multispectral remote sensing imagery," *IEEE Trans. Geosci. Remote Sens.*, vol. 53, no. 7, pp. 3539–3549, Jul. 2015.

[5] J. D. Hedley *et al.*, "Coral reef applications of Sentinel-2: Coverage, characteristics, bathymetry and benthic mapping with comparison to Landsat 8," *Remote Sens. Environ.*, vol. 216, pp. 598–614, Oct. 2018.

[6] D. R. Lyzenga, "Remote sensing of bottom reflectance and water attenuation parameters in shallow water using aircraft and landsat data," *Int. J. Remote Sens.*, vol. 2, no. 1, pp. 71–82, Jan. 1981.

[7] R. P. Stumpf, K. Holderied, and M. Sinclair, "Determination of water depth with high resolution satellite image over variable bottom types," *Limnol. Oceanogr.*, vol. 48, pp. 547–556, Jan. 2003.

[8] P. Vinayaraj, V. Raghavan, and S. Masumoto, "Satellite-derived bathymetry using adaptive geographically weighted regression model," *Mar. Geodesy*, vol. 39, no. 6, pp. 458–478, Oct. 2016.

[9] Y. Liu *et al.*, "Multispectral bathymetry via linear unmixing of the benthic reflectance," *IEEE J. Sel. Top. Appl. Earth Observ. Remote Sens.*, vol. 11, no. 11, pp. 4349–4363, Oct. 2018.

[10] D. R. Lyzenga, "Shallow-water bathymetry using combined lidar and passive multispectral scanner data," *Int. J. Remote Sens.*, vol. 6, no. 6, pp. 115–125, Jan. 1985.

[11] D. R. Lyzenga, N. P. Malinas, and F. J. Tanis, "Multispectral bathymetry using a simple physically based algorithm," *IEEE Trans. Geosci. Remote Sens.*, vol. 44, no. 8, pp. 2251–2259, Sep. 2006.

[12] C. J. Legleiter, D. A. Roberts, W. A. Marcus, and M. A. Fonstad, "Passive optical remote sensing of river channel morphology and in-stream habitat: Physical basis and feasibility," *Remote Sens. Environ.*, vol. 93, no. 4, pp. 493–510, Dec. 2004.

[13] S. Hamylton, J. Hedley, and R. Beaman, "Derivation of high-resolution bathymetry from multispectral satellite imagery: A comparison of empirical and optimisation methods through geographical error analysis," *Remote Sens.*, vol. 7, no. 12, pp. 16257–16273, Dec. 2015.

[14] K. R. Hogrefe, D. J. Wright, and E. J. Hochberg, "Derivation and integration of shallow-water bathymetry:Implications for coastal terrain modeling and subsequent analyses," *Mar. Geodesy*, vol. 31, no. 4, pp. 299–317, Dec. 2008.

[15] J. M. Kerr and S. Purkis, "An algorithm for optically-deriving water depth from multispectral imagery in coral reef landscapes in the absence of ground-truth data," *Remote Sens. Environ.*, vol. 210, pp. 307–324, Mar. 2018.

[16] J. Li *et al.*, "Adaptive bathymetry estimation for shallow coastal waters using planet dove satellites," *Remote Sens. Environ.*, vol. 232, Jul. 2019, Art. no. 111302.

[17] Y. Liu *et al.*, "Rapid estimation of bathymetry from multispectral imagery without in situ bathymetry data," *Appl. Opt.*, vol. 58, no. 27, pp. 7538–7551, Sep. 2019.

[18] M. Lyons, S. Phinn, and C. Roelfsema, "Integrating quickbird multispectral satellite and field data: Mapping bathymetry, seagrass cover, seagrass species and change in Moreton bay, Australia in 2004 and 2007," *Remote Sens.*, vol. 3, no. 1, pp. 42–64, Jan. 2011.

[19] X. Monteys, P. Harris, S. Caloca, and C. Cahalane, "Spatial prediction of coastal bathymetry based on multispectral satellite imagery and multibeam data," *Remote Sens.*, vol. 7, no. 10, pp. 13782–13806, Oct. 2015.

[20] C. M. Bachmann *et al.*, "Bathymetry retrieval from hyperspectral imagery in the very shallow water limit: A case study from the 2007 virginia coast reserve (VCR'07) multi-sensor campaign," *Mar. Geodesy*, vol. 33, no. 1, pp. 53–75, Feb. 2010.

[21] I. Caballero and R. P. Stumpf, "Retrieval of nearshore bathymetry from Sentinel-2A and 2B satellites in South Florida coastal waters," *Estuarine Coastal Shelf Sci.*, vol. 226, Jun. 2019, Art. no. 106277.

[22] P. Bowyer and F. M. Danson, "Sensitivity of spectral reflectance to variation in live fuel moisture content at leaf and canopy level," *Remote Sens. Environ.*, vol. 92, no. 3, pp. 297–308, Aug. 2004.

[23] Z. Lee, K. L. Carder, C. D. Mobley, R. G. Steward, and J. S. Patch, "Hyperspectral remote sensing for shallow waters: 2. Deriving bottom depths and water properties by optimization," *Appl. Opt.*, vol. 38, no. 18, pp. 3831–3843, Jun. 1999.

[24] T. S. Moore, M. D. Dowell, S. Bradt, and A. R. Verdu, "An optical water type framework for selecting and blending retrievals from bio-optical algorithms in lakes and coastal waters," *Remote Sens. Environ.*, vol. 143, no. 143, pp. 97–111, Jan. 2014.

[25] C. Hu, Z. Lee, and B. Franz, "Chlorophyll algorithms for oligotrophic oceans: A novel approach based on three-band reflectance difference," *J. Geophys. Res.*, vol. 117, Jan. 2012, Art. no. C01011.

[26] S. Shang, Z. Lee, G. Lin, Y. Li, and X. Li, "Progressive scheme for blending empirical ocean color retrievals of absorption coefficient and chlorophyll concentration from open oceans to highly turbid waters," *Appl. Opt.*, vol. 58, pp. 3359–3369, May 2019.

[27] M. Wang, S. Son, and L. W. Harding, "Retrieval of diffuse attenuation coefficient in the Chesapeake bay and Turbid ocean regions for satellite ocean color applications," *J. Geophys. Res.*, vol. 114, Oct. 2009, Art. no. C10011.

[28] C. Danilo and F. Melgani, "High-coverage satellite-based coastal bathymetry through a fusion of physical and learning methods," *Remote Sens.*, vol. 11, no. 4, pp. 1–16, Feb. 2019.

[29] B. Chen, Y. Yang, D. Xu, and E. Huang, "A dual band algorithm for shallow water depth retrieval from high spatial resolution imagery with no ground truth," *ISPRS J. Photogramm. Remote Sens.*, vol. 151, pp. 1–13, May 2019.

[30] S. Tang, C. Chen, H. Zhan, and D. Xu, "Remotely-sensed estimation of the euphotic depth in the northern south China sea," presented at the IGRSS, Barcelona, Spain, Jul. 2007, pp. 917–920.

[31] J. Wei *et al.*, "An assessment of Landsat-8 atmospheric correction schemes and remote sensing reflectance products in coral reefs and coastal turbid waters," *Remote Sens. Environ.*, vol. 215, pp. 18–32, Jun. 2018.

[32] M. Iqbal, in *An Introduction to Solar Radiation*. New York, NY, USA: Academic, 1983.

[33] J. D. Hedley, A. R. Harborne, and P. J. Mumby, "Simple and robust removal of sun glint for mapping shallow-water benthos," *Int. J. Remote Sens.*, , vol. 26, no. 10, pp. 2107–2112, May 2005.

[34] C. D. Mobley, in *Light and Water: Radiative Transfer in Natural Waters*. New York, NY, USA: Academic, 1994.

[35] A. V. Griensven, T. Meixner, S. Grunwald, T. Bishop, M. Diluzio, and R. Srinivasan, "A global sensitivity analysis tool for the parameters of multi-variable catchment models," *J. Hydrol.*, vol. 324, no. 1, pp. 10–23, Jun. 2006.

[36] M. Renardy, C. Hult, S. Evans, J. J. Linderman, and D. E. Kirschner, "Global sensitivity analysis of biological multiscale models," *Curr. Opin. Biomed. Eng.*, vol. 11, pp. 109–116, Sep. 2019.

[37] R. M. Pope and E. S. Fry, "Absorption spectrum (380-700 nm) of pure water. II. Integrating cavity measurements," *Appl. Opt.*, vol. 36, no. 33, pp. 8710–8723, Nov. 1997.

[38] Z. Lee, K. L. Carder, C. D. Mobley, R. G. Steward, and J. S. Patch, "Hyperspectral remote sensing for shallow waters. I. A semianalytical model," *Appl. Opt.*, vol. 37, no. 27, pp. 6329–6338, Sep. 1998.

[39] S. Maritorena and D. A. Siegel, "Consistent merging of satellite ocean color data sets using a bio-optical model," *Remote Sens. Environ.*, vol. 94, no. 4, pp. 429–440, Feb. 2005.

[40] A. Bricaud, M. Babin, A. Morel, H. Eacute, and C. Eacute, "Variability in the chlorophyll-specific absorption coefficients of natural phytoplankton: Analysis and parameterization," *J. Geophys. Res.*, vol. 100, no. C7, pp. 13321–13332, Jul. 1995.

[41] T. Petit, T. Bajjouk, P. Mouquet, S. Rochette, B. Vozel, and C. Delacourt, "Hyperspectral remote sensing of coral reefs by semi-analytical model inversion – Comparison of different inversion setups," *Remote Sens. Environ.*, vol. 190, pp. 348–365, Jan. 2017.

[42] C. J. Legleiter and D. A. Roberts, "A forward image model for passive optical remote sensing of river bathymetry ☆," *Remote Sens. Environ.*, vol. 113, no. 5, pp. 1025–1045, May 2009.

[43] I. N. Figueiredo, L. Pinto, and G. Goncalves, "A modified Lyzenga's model for multispectral bathymetry using Tikhonov regularization," *IEEE Geocsi. Remote S.*, vol. 13, no. 1, pp. 1–5, Jan. 2015.

[44] G. Casal, J. Hedley, X. Monteys, P. Harris, C. Cahalane, and T. McCarthy, "Satellite-derived bathymetry in optically complex waters using a model inversion approach and Sentinel-2 data," *Estuarine Coastal Shelf Sci.*, May 2020, Art. no. 106814.

Yongming Liu received the B.S. degree in geographic information system from China University of Geosciences, Wuhan, China, in 2014, and the Ph.D. degree in cartography and geographic information system from Sun Yat-sen University, Guangzhou, China, in 2019.

He is currently a Postdoc Researcher with the South China Sea Institute of Oceanology, Chinese Academy of Sciences, Guangzhou, China. His research interests include remote sensing of coral reefs and inland waters.

Danling Tang received the Ph.D. degree in biology from Hong Kong University of Science and Technology, Hong Kong, China.

She is the Director of Guangdong Key Lab of Ocean Remote Sensing, China and has been working for Southern Marine Science and Engineering Guangdong Laboratory (Guangzhou), and South China Sea Institute of Oceanology, Chinese Academy of Sciences. She has conducted research and teaching in USA, Hong Kong, and Japan. She has been at the forefront of scientific research for a long time, engaged in basic research of ocean satellite remote sensing, and has authored or coauthored approximately SCI 150 papers, and books "*Remote Sensing of the Changing Oceans*" and "*Typhoon Impact and Crisis Management*" by Springer. She proposed a conceptual model of "Wind Pump" to assess role of wind-induced advection transport in phytoplankton bloom formation and typhoon impacts on marine ecosystem. She has serviced for scientific communities: The President of the Pan Ocean Remote Sensing Association, the President of PACON International, Councilor of AGU, and Vice Chair of A2 Commission, Committee on Space Research, etc. Her scientific achievements have been repeatedly highlighted in the ICSU journal "*Space Research Today*". Her research interests include application of satellite remote sensing for marine ecology/environment, ocean dynamics of phytoplankton ecology, remote sensing of natural hazard and disaster management, and global environmental changes.

Ruru Deng received the B.S. degree in geology from Wuhan College of Geology, Wuhan, China, in 1984, the M.E. degree in remote sensing geology from China University of Geosciences, Wuhan, China, in 1989, and the Ph.D. degree in microwave remote sensing from the Institute of Remote Sensing and Digital Earth, Chinese Academy of Sciences, Beijing, China, in 2002.

He is currently a Professor with Sun Yat-sen University, Guangzhou, China. His research interests include atmospheric correction of optical remote sensing data, quantitative remote sensing of inland waters and coral reefs, and application development to microwave remote sensing.

Bin Cao received the bachelor's degree in electronic and information engineering from Zhengzhou University, Zhengzhou, China, in 2015, and the master's degree in environmental science and engineering from Shanghai Ocean University, China, in 2018. He is currently working toward the Ph.D. degree at the School of Geography and Planning, Sun Yat-sen University, Guangzhou, China.

His research interests include optical remote sensing and bathymetry.

Qidong Chen received the B.S. degree from Anhui Normal University, Wuhu, China, in 2005, the M.S. and Ph.D. degrees from School of Geography and Planning, Sun Yat-sen University, Guangzhou, China, in 2009 and 2014 respectively.

He is with the South China Sea Institute of Planning and Environmental Research, State Oceanic Administration, Guangzhou, China. His research interests include remote sensing of ocean color and water depth.

Yan Qin received the B.S. degree in geographic information system and the Ph.D. degree in cartography and geographic information system from Sun Yat-sen University, Guangzhou, China, in 2007and 2015, respectively.

She is currently an Engineer with the Guangdong Research Institute of Water Resources and Hydropower, Guangzhou, China. Her research interests include remote sensing of the water environment and air pollution.

Ruihao Zhang received the B.Sc. and M.Sc. degrees in geographic information system and human geography from South China Normal University, Guangzhou, China, in 2014 and 2017, respectively. He is currently working toward the Ph.D. degree with the School of Geography and Planning, Sun Yat-sen University, Guangzhou, China.

His research interests include machine/statistical learning, nonconvex optimization and their applications in hyperspectral unmixing, and ocean color remote sensing.

Shaoquan Zhang received the B.S. and M.E. degrees from Nanchang Institute of Technology, Nanchang, China, in 2012 and 2015, respectively, and the Ph.D. degree from the Sun Yat-sen University, Guangzhou, China, in 2018.

He is currently a Lecturer with Jiangxi Province Key Laboratory of Water Information Cooperative Sensing and Intelligent Processing, Nanchang Institute of Technology, Nanchang, China. His research interests include hyperspectral unmixing, sparse representation, and machine learning.